Original Article

A non-dimensional study of the flow through co-rotating discs and performance optimization of a Tesla disc turbine

Abhijit Guha and Sayantan Sengupta

Abstract

This article presents a systematic and comprehensive computational fluid dynamic study for co-rotating discs and, Tesla turbines, in which the full benefit of similitude and scaling is extracted by expressing the results and analyses in terms of carefully formulated non-dimensional numbers—five input parameters and three output parameters. The work formulates a systematic design methodology for the optimum selection of input parameters for the rotor of a Tesla disc turbine that would satisfy practical constraints and deliver high values of power and efficiency. Many subtle flow physics (e.g. the identification of dynamic similarity number, inlet tangential speed ratio and inlet flow angle as the three most important non-dimensional input parameters, the secondary role of aspect ratio as a separate quantity independent of dynamic similarity number, and, the variation in the four fundamental components of the radial pressure difference) are critically explained. The present study establishes, for the first time, that unlike the flow in a conventional turbomachine in which fluid friction plays only a detrimental role, fluid friction plays a dual role in a Tesla disc turbine—a detrimental role in increasing the radial pressure drop (thus tending to decrease the efficiency) and a beneficial role by providing the sole mechanism for power production. This dual role is comprehensively analyzed and quantified in this work. The balance between this dual role of fluid friction gives rise to the optimum values of dynamic similarity number and inlet tangential speed ratio that maximize efficiency.

Introduction

In a recent article,[1] a systematic study of similitude and scaling laws was undertaken for the flow through co-rotating discs with inflow, which is found in a Tesla disc turbine. This study[1] established, through careful formulation and powerful demonstration, the required non-dimensional numbers for describing the flow and for evaluating the performance—five input parameters ($\hat{r}_o$, $\hat{b}$, γ, α, Ds) and three output parameters ($\hat{W}$, $\Delta\hat{p}_{io}$, η) in total. The actual quantitative dependence of the fluid dynamics and performance on the input variables such as Ds, γ, and $\hat{b}$ has been determined here through a comprehensive set of computations which involve about 1000 separate computational fluid dynamic (CFD) simulations, each run to a high degree of convergence (the "scaled" residual for all conserved variables is set as 10^{-10}, which is much smaller than what is normally set in much of

the reported CFD work). This comprehensiveness and precision have helped us to formulate generic principles, identify subtle physical mechanisms, and develop optimisation strategies.

The principle of similitude established in Guha and Sengupta[1] is summarized below for ready reference. For geometric similarity between the model tested and the prototype to be designed, the radius ratio $\hat{r}_o$ and aspect ratio $\hat{b}$ of the model should be the same as that of the prototype. For kinematic similarity between a geometrically similar model and the prototype, the

Mechanical Engineering Department, Indian Institute of Technology Kharagpur, Kharagpur, West Bengal, India

Corresponding author:
Sayantan Sengupta, Mechanical Engineering Department, Indian Institute of Technology Kharagpur, Kharagpur 721302, West Bengal, India.
Email: sayantansengupta@iitkgp.ac.in

tangential speed ratio at inlet γ and the flow angle at inlet α of the model should be the same as those of the prototype. After achieving both geometric and kinematic similarities, the attainment of dynamic similarity further requires that the dynamic similarity number Ds used for the model should be the same as that of the prototype. When dynamic similarity is achieved, the principle of similitude enunciates that the power coefficient $\hat{W}$ and the pressure difference coefficient $\Delta\hat{p}_{io}$ of a model would be the same as those of the prototype.

A Tesla disc turbine is a power producing device which was invented by the famous scientist Nikola Tesla in 1913.[2] Hundred years after the invention of Tesla turbine, it is still not a favorite candidate in the power industry. A major drawback is the low efficiency of several experimental machines built and tested in various parts of the world. A Tesla disc turbine has two major components, namely the inlet nozzle assembly and the rotor. Guha and Smiley[3] developed an improved design of the nozzle, greatly improving the efficiency and achieving uniformity in the velocity profile of the jet. (The loss in the nozzle is generally recognized[4,5] as a major source of loss in the conventional designs of a Tesla turbine.) In this paper, a detailed investigation is conducted with the aim to design an efficient rotor. Unlike a bladed turbine (many details and a systematic optimization study on gas turbines are presented in Guha[6,7]), the rotor of a Tesla turbine is constructed by a series of flat, parallel, co-rotating discs which are attached to a central shaft. The inter-disc-spacing is usually small (of the order of 100 μm). The working fluid, which is injected nearly tangentially to the periphery of the rotor, passes through the narrow inter-disc-spacings moving spirally towards the exhaust-port located at the disc-center. There is a stationary housing surrounding the rotor. A small radial and axial clearance is maintained between the rotor and the stationary housing. The Tesla disc turbine has several advantages. Other than its manufacturing simplicity and low cost, the Tesla disc turbine is capable of generating power with a variety of working media like Newtonian fluids, non-Newtonian fluids, mixed fluids, and two-phase mixtures (a body of relevant physics of two-phase flow is available in Guha[8,9]). In the case of nonconventional fuels like biomass, which produce solid particles, or, in the case of low quality wet steam operating condition producing vapor–droplet mixture (which may be encountered while utilizing geothermal energy or low-grade waste heat energy), conventional turbines may suffer from blade erosion. In such operating conditions, a bladeless Tesla turbine may be suitable due to its self-cleaning nature.

A summary of the major investigations up to 1991 regarding a Tesla disc turbine is found in the study by Rice.[5] Experimental, theoretical, and computational studies are still being reported in this field. Detailed experimental studies are available in Guha and Smiley,[3] Lemma et al.,[10] and Hoya and Guha.[11] An effective technique for measuring the net power output and overall loss called the angular acceleration method was developed by Hoya and Guha,[11] which is particularly useful for high angular speed and low-torque operating conditions. Theoretical approaches for predicting the performance of a Tesla disc turbine are discussed in various references.[12–15] A computational study regarding the Tesla disc turbine is reported in Sengupta and Guha.[16] Descriptions of various investigations regarding the flow in and performance of a Tesla disc turbine are also available in many dissertations.[17–25] A systematic attempt of experimentally determining (hence optimizing) turbine performance as functions of various parameters such as disc spacing, number of discs, inlet flow angle, nozzle area, rotational speed, etc. is described in McGarey and Monson.[22] The present non-dimensional optimization study is however comprehensive and unique; we could not find a similar study in the available literature including the dissertations.[17–25]

Studies of flow above a rotating disc,[26–29] flow between a stator and a rotor,[30–33] and flow through co-rotating discs[34–36] are worth mentioning here since the subject-matter is connected. The fluid dynamics of the flow through the co-rotating discs of a Tesla disc turbine, however, is not as widely discussed as it is for the von Kármán's flow[26] and the Batchelor's flow.[30] Guha and Sengupta[13] explained some interesting and intriguing fluid dynamic aspects (e.g. flow reversal, complex pathlines, subtle role of Coriolis acceleration, etc.), which are involved in the flow through co-rotating discs of a Tesla disc turbine. The fluid dynamics of work transfer from the working fluid to disc-surfaces for this rotating-flow is given in Guha and Sengupta.[15]

In this paper, the power of similitude and dimensional analysis is combined with the power of computational fluid dynamics to formulate, from a large set of accurate numerical simulations, a generalized procedure for designing the best possible rotor of a Tesla disc turbine. The synthesis of physical principles for the fluid flow within co-rotating discs leads to design optimization of Tesla disc turbines, thus establishing here a connection between the interest of a fluid dynamicist and the goal of an engineer. Unlike the flow in a conventional turbomachine in which fluid friction plays only a detrimental role, fluid friction plays a dual role in a Tesla disc turbine—a detrimental role in increasing the radial pressure drop (thus tending to decrease the efficiency) and a beneficial role by providing the sole mechanism for power production. This dual role is comprehensively analysed and quantified in this work.

Mathematical formulation

In this section, a mathematical analysis for flow through co-rotating discs of a Tesla disc turbine is

provided. This theoretical framework is required for the physical interpretation and understanding of the numerical results generated through CFD simulations. Figure 1(a) shows the physical configuration showing two circular rotor discs separated axially (i.e. in the z-direction) by a distance b. The rotor inlet is situated along the periphery of the discs (i.e. at radius r_i). The rotor outlet is at the center of the discs (at radius r_o).

This section is divided into four subsections. In the first section, governing differential equations and suitable boundary conditions for flow through the co-rotating discs are provided. In the second, the components of radial pressure difference in a relative frame of reference are identified. In the third, the appropriate non-dimensional numbers to describe the present flow physics are provided. Finally, the definitions of power output and efficiency of a Tesla turbine are given.

Governing equations and boundary conditions

The analysis is based on Navier–Stokes equations in cylindrical coordinate system for steady, laminar, incompressible, axisymmetric flow of a Newtonian fluid with constant density and viscosity. The assumed
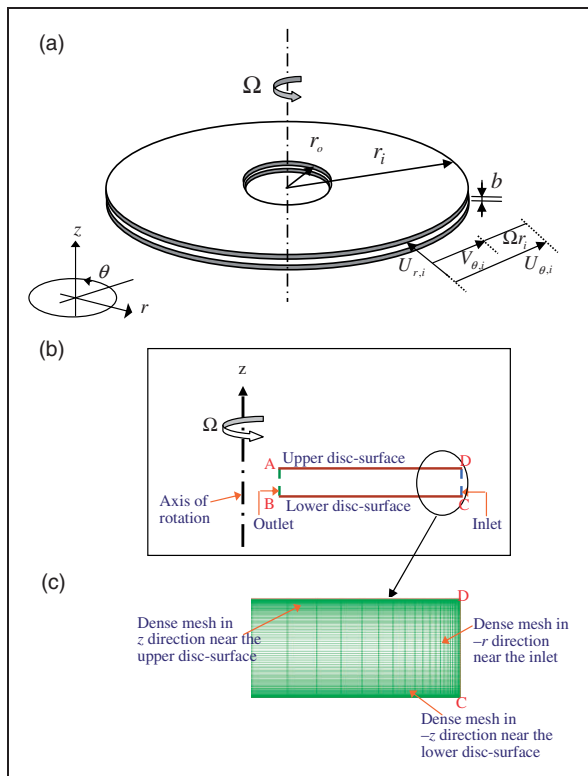

Figure 1. Schematic diagram of the physical configuration, 2D computational domain, and computational mesh: (a) the physical configuration of a Tesla disc turbine showing only two discs; (b) 2D computational domain (ABCD) used in the axisymmetric CFD simulations; (c) details of mesh near the inlet. (The gap within the two discs, in relation to the radius, is exaggerated in the sketch for clarity.)

orientation of the discs is such that gravity acts in the negative z-direction, i.e. both g_θ and g_r are zero. The governing equations[1] are given as follows

$$\frac{1}{r}\frac{\partial(rU_r)}{\partial r} + \frac{\partial U_z}{\partial z} = 0 \tag{1}$$

$$\rho\left(U_r\frac{\partial U_r}{\partial r} - \frac{U_\theta^2}{r} + U_z\frac{\partial U_r}{\partial z}\right)$$
$$= -\frac{\partial p}{\partial r} + \mu\left[\frac{1}{r}\frac{\partial}{\partial r}(r\frac{\partial U_r}{\partial r}) - \frac{U_r}{r^2} + \frac{\partial^2 U_r}{\partial z^2}\right] \tag{2}$$

$$\rho\left(U_r\frac{\partial U_\theta}{\partial r} + \frac{U_r U_\theta}{r} + U_z\frac{\partial U_\theta}{\partial z}\right)$$
$$= \mu\left[\frac{1}{r}\frac{\partial}{\partial r}(r\frac{\partial U_\theta}{\partial r}) - \frac{U_\theta}{r^2} + \frac{\partial^2 U_\theta}{\partial z^2}\right] \tag{3}$$

$$\rho\left(U_r\frac{\partial U_z}{\partial r} + U_z\frac{\partial U_z}{\partial z}\right)$$
$$= -\frac{\partial p}{\partial z} + \rho g_z + \mu\left[\frac{1}{r}\frac{\partial}{\partial r}(r\frac{\partial U_z}{\partial r}) + \frac{\partial^2 U_z}{\partial z^2}\right] \tag{4}$$

Equations (1) to (4) are solved for the following boundary conditions

at $z = 0$ and b, $U_r = 0$, $U_\theta = \Omega r$, $U_z = 0$ (5)

at $r = r_i$, $U_r = U_{r,i}$, $U_\theta = U_{\theta,i}$, $U_z = 0$ (6)

at $r = r_o$, $p = 0$ (7)

The surfaces of the two discs are at $z = 0$ and $z = b$; equation (5) refers to the no-slip and no-penetration boundary conditions. At the outlet, a zero gauge pressure is specified (equation (7)). At the inlet, three components of velocity are specified (equation (6)). In equation (6), both the radial velocity $U_{r,i}$ and the tangential velocity $U_{\theta,i}$ are independent of θ. We consider axisymmetric inflow condition all along the periphery of the rotor. For a Tesla disc turbine, axisymmetric flow can be either approached by increasing the number of discrete nozzles at rotor inlet or achieved by using a plenum chamber at the rotor inlet. Previous researchers used both methods in their experimental studies. We adopt the physical configuration of the experimental set-up given in Lemma et al.[10] in which a plenum chamber is used to achieve axisymmetric inflow condition. In this practicable way, we keep our focus here on the important question about how to design the best possible rotor of a Tesla disc turbine, segregating it from the issue of nozzle–rotor interaction in the case of a small number of discrete nozzles. Almost all of the published journal articles use the axisymmetric inflow condition for theoretical modeling. In a previous publication,[12] we have demonstrated that our theoretical predictions for turbine performance match well with the experimental results.

Components of radial pressure difference in a relative frame of reference

Consider a relative frame of reference in which the observer is rotating at the same angular velocity as that of the disc, denoted by Ω. The relations between the components of velocity in absolute frame (U_r, U_z, and U_θ) and the components of velocity in the relative frame (V_r, V_z, and V_θ) are as follows

$$U_r = V_r; \quad U_z = V_z; \quad U_\theta = (V_\theta + \Omega r) \tag{8}$$

Substituting equation (8) into equation (2), the following equation is obtained

$$\frac{\partial p}{\partial r} = \left(\frac{\rho V_\theta^2}{r} - \rho V_r \frac{\partial V_r}{\partial r} - \rho V_z \frac{\partial V_r}{\partial z} \right) + 2\rho \Omega V_\theta + \rho \Omega^2 r$$
$$+ \mu \left[\frac{1}{r} \frac{\partial}{\partial r} \left(r \frac{\partial V_r}{\partial r} \right) - \frac{V_r}{r^2} + \frac{\partial^2 V_r}{\partial z^2} \right] \tag{9}$$

Equation (9) can be interpreted as a relation between the radial pressure gradient ($\frac{\partial p}{\partial r}$) and the terms obtained from various forces. The integral form of equation (9) is as follows

$$\frac{1}{b} \int_{r_i}^{r_o} \int_0^b \frac{\partial p}{\partial r} \delta z \delta r$$
$$= \int_{r_i}^{r_o} \left(\frac{1}{b} \int_0^b \left(\frac{\rho V_\theta^2}{r} - \rho V_r \frac{\partial V_r}{\partial r} - \rho V_z \frac{\partial V_r}{\partial z} \right) \delta z \right) \delta r$$
$$+ \int_{r_i}^{r_o} \left(\frac{1}{b} \int_0^b (2\rho \Omega V_\theta) \delta z \right) \delta r$$
$$+ \int_{r_i}^{r_o} \left(\frac{1}{b} \int_0^b (\rho \Omega^2 r) \delta z \right) \delta r +$$
$$+ \int_{r_i}^{r_o} \left(\frac{1}{b} \int_0^b \left(\mu \left[\frac{1}{r} \frac{\partial}{\partial r} \left(r \frac{\partial V_r}{\partial r} \right) - \frac{V_r}{r^2} + \frac{\partial^2 V_r}{\partial z^2} \right] \right) \delta z \right) \delta r \tag{10}$$

Various terms in equation (10) are expressed below with their physical interpretations.

$$\frac{1}{b} \int_{r_i}^{r_o} \int_0^b \frac{\partial p}{\partial r} \delta z \delta r = \frac{1}{b} \int_0^b \int_{r_i}^{r_o} \frac{\partial p}{\partial r} \delta r \delta z = \Delta p_{io} \tag{11}$$

$$\int_{r_i}^{r_o} \left(\frac{1}{b} \int_0^b \left(\frac{\rho V_\theta^2}{r} - \rho V_r \frac{\partial V_r}{\partial r} - \rho V_z \frac{\partial V_r}{\partial z} \right) \delta z \right) \delta r$$
$$= \Delta p_{io,inertia} \tag{12}$$

$$\int_{r_i}^{r_o} \left(\frac{1}{b} \int_0^b (2\rho \Omega V_\theta) \delta z \right) \delta r = \Delta p_{io,Coriolis} \tag{13}$$

$$\int_{r_i}^{r_o} \left(\frac{1}{b} \int_0^b (\rho \Omega^2 r) \delta z \right) \delta r = \Delta p_{io,centrifugal} \tag{14}$$

$$\int_{r_i}^{r_o} \left(\frac{1}{b} \int_0^b \left(\mu \left[\frac{1}{r} \frac{\partial}{\partial r} (r \frac{\partial V_r}{\partial r}) - \frac{V_r}{r^2} + \frac{\partial^2 V_r}{\partial z^2} \right] \right) \delta z \right) \delta r$$
$$= \Delta p_{io,viscous} \tag{15}$$

The overall pressure difference between outlet and inlet is denoted by Δp_{io}. Equations (12) to (15) show the expressions of various components of Δp_{io}. In equation (12), $\Delta p_{io,inertia}$ indicates the pressure difference due to inertia force (the contributions of Coriolis and centrifugal forces are taken separately, and these are not included in $\Delta p_{io,inertia}$). In equation (13), $\Delta p_{io,Coriolis}$ signifies the pressure difference due to Coriolis force; in equation (14), $\Delta p_{io,centrifugal}$ signifies the pressure difference due to centrifugal force; and, in equation (15), $\Delta p_{io,viscous}$ indicates pressure difference due to viscous force.

Non-dimensional numbers and non-dimensional equations

A systematic dimensional analysis, a similitude study, and, the proper scaling laws for arriving at simplified conservation equations are provided in Guha and Sengupta.[1] In the study,[1] seven non-dimensional numbers of importance (for a Tesla disc turbine) have been identified

Radius ratio: $\quad \hat{r}_o = \dfrac{r_o}{r_i} \tag{16}$

Aspect ratio: $\quad \hat{b} = \dfrac{b}{r_i} \tag{17}$

Tangential speed ratio at inlet: $\quad \gamma = \dfrac{\bar{U}_{\theta,i}}{\Omega r_i} \tag{18}$

Flow angle at inlet: $\quad \alpha = \tan^{-1} \dfrac{|\bar{U}_{r,i}|}{\bar{U}_{\theta,i}} \tag{19}$

Dynamic similarity number: $\quad Ds = \dfrac{b}{r_i} \left(\dfrac{|\bar{U}_{r,i}| b}{\nu} \right) \tag{20}$

Power coefficient: $\quad \hat{\dot{W}} = \dfrac{\dot{W}}{(\rho |\bar{U}_{r,i}|^3 r_i^2)} \tag{21}$

Pressure difference coefficient: $\quad \Delta \hat{p}_{io} = \dfrac{\Delta p_{io}}{\rho \bar{U}_{\theta,i}^2} \tag{22}$

In the CFD simulations, $\hat{r}_o$, $\hat{b}$, γ, α, and Ds are used as the input; and $\hat{\dot{W}}$ and $\Delta \hat{p}_{io}$ are the output. In equations (18) to (22), sectional average values of the tangential and radial velocities, denoted by the symbol overbar, are used. $\bar{U}_\theta(r)$ is defined as $\bar{U}_\theta(r) = (1/b) \int_0^b U_\theta dz$ and $\bar{U}_r(r)$ is defined as

$\overline{U}_r(r) = (1/b)\int_0^b U_r dz$. Thus, in equations (18) to (22), $\overline{U}_{\theta,i}$ is the value of $\overline{U}_\theta(r)$ at the inlet, i.e. at $r = r_i$. Similarly, $\overline{U}_{r,i}$ is the value of $\overline{U}_r(r)$ at the inlet, i.e. at $r = r_i$.

In addition to the above non-dimensional numbers, the following non-dimensional variables are provided as follows[1]

$$\hat{r} = \frac{r}{r_i}, \quad \hat{z} = \frac{z}{b}, \quad \hat{U}_\theta = \frac{U_\theta}{\Omega r_i}, \quad \hat{U}_r = \frac{U_r}{|\bar{U}_{r,i}|},$$

$$\hat{U}_z = \frac{U_z}{|\bar{U}_{r,i}|}\frac{r_i}{b}, \quad \hat{p} = \frac{p}{\rho \bar{U}_{\theta,i}^2} \tag{23}$$

These non-dimensional variables (equation (23)) and the above nondimensional numbers (equations (16) to (22)) are used to represent the conservation equations (1) to (4) in a non-dimensional form. The non-dimensional equation set is given below.

$$\frac{1}{\hat{r}}\frac{\partial(\hat{r}\hat{U}_r)}{\partial \hat{r}} + \frac{\partial \hat{U}_z}{\partial \hat{z}} = 0 \tag{24}$$

$$\hat{U}_r\frac{\partial \hat{U}_r}{\partial \hat{r}} + \hat{U}_z\frac{\partial \hat{U}_r}{\partial \hat{z}} - \frac{\hat{U}_\theta^2}{\hat{r}(\gamma\tan\alpha)^2}$$
$$= -\frac{1}{(\tan\alpha)^2}\frac{\partial \hat{p}}{\partial \hat{r}} + \frac{1}{Ds}\left[\frac{\partial^2 \hat{U}_r}{\partial \hat{z}^2} + \hat{b}^2\left(\frac{1}{\hat{r}}\frac{\partial}{\partial \hat{r}}(\hat{r}\frac{\partial \hat{U}_r}{\partial \hat{r}}) - \frac{\hat{U}_r}{\hat{r}^2}\right)\right] \tag{25}$$

$$\hat{U}_r\frac{\partial \hat{U}_\theta}{\partial \hat{r}} + \hat{U}_z\frac{\partial \hat{U}_\theta}{\partial \hat{z}} + \frac{\hat{U}_r\hat{U}_\theta}{\hat{r}}$$
$$= \frac{1}{Ds}\left[\frac{\partial^2 \hat{U}_\theta}{\partial \hat{z}^2} + \hat{b}^2\left(\frac{1}{\hat{r}}\frac{\partial}{\partial \hat{r}}(\hat{r}\frac{\partial \hat{U}_\theta}{\partial \hat{r}}) - \frac{\hat{U}_\theta}{\hat{r}^2}\right)\right] \tag{26}$$

$$\hat{U}_r\frac{\partial \hat{U}_z}{\partial \hat{r}} + \hat{U}_z\frac{\partial \hat{U}_z}{\partial \hat{z}}$$
$$= -\frac{1}{\hat{b}^2(\tan\alpha)^2}\left(\frac{\partial \hat{p}'}{\partial \hat{z}}\right)$$
$$+ \frac{1}{Ds}\left[\hat{b}^2\left(\frac{1}{\hat{r}}\frac{\partial}{\partial \hat{r}}(\hat{r}\frac{\partial \hat{U}_z}{\partial \hat{r}})\right) + \frac{\partial^2 \hat{U}_z}{\partial \hat{z}^2}\right] \tag{27}$$

In equation (27), p' is the modified pressure, which is equal to $(p - \rho g_z z)$.

Power output and efficiency of a Tesla turbine

The power output due to viscous drag for the fluid flow between two successive discs can be expressed as $\dot{W} = 2\Gamma_{shear}\Omega$, where Γ_{shear} is the torque produced by one side of a single disc.[15] In reality, a Tesla turbine consists of multiple discs. The total power output of a rotor consisting of n discs is given by

$$\dot{W} = 2(n-1)\Gamma_{shear}\Omega \tag{28}$$

All results given in the present paper correspond to $n = 2$.

Sengupta and Guha[12] have given a closed-form analytical solution of equations (24) to (27) by invoking several assumptions (such as, the velocity distributions at inlet are parabolic, the value of Ds is small, etc.). The analytical solution was validated with the experimental data given in Lemma et al.[10] According to the analytical theory, the closed-form expression for Γ_{shear} can be expressed in terms of Ds, γ, and $\hat{r}_o$ as follows

$$\Gamma_{shear} = \frac{12\pi\mu\overline{V}_{\theta,i}r_i^3}{b}\left[\frac{Ds}{12(\gamma-1)}(1-\hat{r}_o^2)\right.$$
$$\left. + \frac{Ds}{10}\left(1 - \frac{Ds}{6(\gamma-1)}\right)\left\{1 - \exp\left[-\frac{5}{Ds}(1-\hat{r}_o^2)\right]\right\}\right] \tag{29}$$

(There is a typographical error in the equation for Γ_{shear} given in Guha and Sengupta[1] where Ds got replaced, by mistake, by $-Ds$.) The accuracy of equation (29), for small values of Ds, is established in the Appendix. The present CFD simulations provide numerical values of Γ_{shear} for the entire ranges of non-dimensional parameters.

Previous researchers defined the efficiency (η) of a Tesla turbine in various ways.[11] From these possibilities, the following definition of efficiency is adopted here for the numerical illustrations

$$\eta = \frac{\dot{W}}{Q\left(p_i + 0.5\rho\left(U_{\theta,i}^2 + U_{r,i}^2\right)\right)} \tag{30}$$

In equation (30), Q $(= -2\pi r_i b U_{r,i})$ is the volume flow rate between two successive discs; and $(p_i + 0.5\rho(U_{\theta,i}^2 + U_{r,i}^2))$ is the gauge value of total pressure at inlet. In the CFD simulations, a zero gauge pressure is specified at the outlet i.e. $p_o = 0$ Pa; and, the gauge pressure at the inlet (p_i) is obtained as the output. With the particular value specified at the outlet boundary, the inlet gauge pressure becomes equal to the overall pressure difference between the outlet and the inlet i.e. $p_i = |\Delta p_{io}|$. The denominator of equation (30) signifies the power input to the rotor.

CFD Simulations

Figure 1(a) shows the relevant fluid flow domain, which is three dimensional. However, considering the axisymmetry of the flow field (see section "Governing equations and boundary conditions"), the present computation has been performed in a two-dimensional geometry with appropriate equations for axisymmetric flow (equations (1) to (4)). The two-dimensional geometry is a $r - z$ plane between the two discs. It is to be remembered that the axisymmetric assumption means that the

Table 1. Grid independence test (for $\hat{r}_o = 0.528$, $\hat{b} = 0.008$, $\gamma = 1.25$, $\alpha = 6.2°$, $Ds = 1.26$ and UVDI).

Grid distribution	Number of grids in the r- and z-directions	Total number of grids	Pressure difference coefficient, $\Delta\hat{p}_{io}$	Power coefficient, $\hat{W}$
Coarse	(75×50)	3750	−0.615182	1.941514
Standard	(125×100)	12500	−0.615817	1.947041
Fine	(200×150)	30000	−0.615944	1.948746

Results are shown to 6 decimal places so that the smallness of the difference between the solutions with standard and fine grids can be appreciated. UVDI: Uniform velocity distribution at inlet.

circumferential gradients of all flow variables are zero, there is no requirement that the circumferential or tangential velocity is zero. In fact, the tangential velocity plays a crucial role in the fluid dynamics of Tesla disc turbine. Note that the axisymmetric version of the conservation equations, namely equations (1) to (4), contains all three components of the velocity, namely the radial component U_r, tangential component U_θ, and z-component U_z. Accordingly, boundary values for the three components are specified at the inlet face CD shown in Figure 1(b). The solution of equations (1) to (4) then determines the three components at all other points of the $r − z$ plane shown in Figure 1(b).

The governing equations are solved by a commercially available CFD software Fluent 6.3.26. Two-dimensional, steady, double precision, pressure based and implicit solver is used. The velocity formulation is in the absolute frame of reference. "Axisymmetric swirl model"[37] is utilized to solve the flow field. We consider laminar flow (a discussion on the transition from laminar to turbulence within the inter-disc-spacing of a Tesla turbine is given in Guha and Sengupta;[13,15] the flow remains laminar unless Ds exceeds 10; in the present study, Ds is kept much less than 10). The SIMPLE algorithm, with second order upwind scheme for momentum and the "Standard"[37] pressure interpolation scheme, is used. Under-relaxation factors for momentum (radial and axial components), swirl (tangential component), pressure, density, and body force are selected as 0.7, 0.9, 0.3, 1, and 1, respectively. The convergence criterion for the maximum "scaled" residual[37] for all conserved variables is set as 10^{-10}.

The geometry of the computational domain and the grid (in r and z directions) are constructed by a commercially available software GAMBIT 2.4.6. We consider the flow within two successive discs separated by a small gap (b). Each disc has an inlet radius (r_i) and an outlet radius (r_o). The boundary conditions (equations (5) to (7)) given in section "Governing equations and boundary conditions" are implemented in the axisymmetric CFD simulations in the following way. Figure 1(b) shows the axisymmetric computational domain. In Figure 1(b), AB is the outlet (at $r = r_o$), CD is the inlet (at $r = r_i$), BC is the lower disc surface ($z = 0$), and AD is the upper disc surface ($z = b$). At the inlet, both tangential and radial components of velocity are specified (equation (6)); and the z-component of velocity is

zero (equation (6)). The outlet boundary condition is modeled by the "pressure outlet" option offered by Fluent, with zero gauge pressure (equation (7)). No-slip (for U_r and U_θ) and no-penetration (for U_z) boundary conditions (equation (5)) are applied on the disc surfaces. A nonzero rotational speed (Ω) of the discs is also set.

A grid independence test has been carried out (Table 1 showing a few pertinent details), and based on this study, a total 12,500 (125×100) mapped, quadrilateral computational cells are used for the results presented in this paper. The grids are distributed in r- and z-directions in accordance with the difference in the flow physics in the two directions. The grid distribution in the z-direction is nonuniform with very small grid size close to the surfaces of the two discs (to capture the velocity gradient on the surface accurately) and with progressively larger grid size as one moves away from the surfaces to the middle of the inter-disc gap (with a successive ratio of 1.05). In order to properly capture the rapid change of velocity profiles near the inlet,[15] the grids in the radial direction are divided into two zones—nonuniform and uniform. Near the inlet, nonuniform boundary-layer-type grids with 25 rows in the radial direction are used (Figure 1(c)). The size of the first grid is 0.001 mm and the successive ratio of the geometric progression series is 1.2. The rest of the radial extent up to the outlet is meshed uniformly with 100 grid points. The non-dimensional parameters for obtaining the results shown in Table 1 are given in the caption of Table 1. The table shows the computed values of two important output parameters $\Delta\hat{p}_{io}$ (pressure difference coefficient) and $\hat{W}$ (power coefficient) for three different grid distributions (coarse, standard and fine). As the grid is changed from coarse to standard $\Delta\hat{p}_{io}$ changes by −0.10307% and $\hat{W}$ changes by −0.28388%. These values are respectively 0.020716% and 0.087567% as the grid is changed from standard to fine. Thus, a marginal change of $\Delta\hat{p}_{io}$ and $\hat{W}$ is observed after attaining the "standard" grid distribution containing 12,500 computational cells (125×100). On the basis of the grid independence test, all results given in this paper are obtained by using the grid distribution of 125×100.

In order to achieve a comprehensive study of the various non-dimensional numbers, an extraordinarily

Table 2. Verification of CFD simulations based on the axisymmetric formulation (for $\hat{r}_o = 0.528$, $\hat{b} = 0.008$, $\gamma = 1.25$, $\alpha = 6.2°$, $Ds = 1.26$).

Velocity distributions at inlet	Method	Pressure difference coefficient, $\Delta\hat{p}_{io}$	Power coefficient, $\hat{W}$
UVDI $(U_{\theta,i} = \overline{U}_{\theta,i}$ and $U_{r,i} = \overline{U}_{r,i})$	CFD simulation based on the axisymmetric formulation	−0.615817	1.947041
	Three-dimensional CFD simulation	−0.615899	1.947484
PVDI $(U_{\theta,i} = \overline{V}_{\theta,i}[6(z/b)(1-z/b)] + \Omega r_i$ and $U_{r,i} = \overline{U}_{r,i}[6(z/b)(1-z/b)])$	CFD simulation based on the axisymmetric formulation	−0.637421	2.059629
	Three-dimensional CFD simulation	−0.637501	2.060065

Results are shown to 6 decimal places so that the smallness of the difference between axisymmetric and 3D simulations can be appreciated.
CFD: computational fluid dynamics; UVDI: uniform velocity distribution at inlet; PVDI: parabolic velocity distribution at inlet.

large number of separate computational simulations (of the order 1000) has been performed in the present work. Hence, the method of three-dimensional CFD simulation for flow through co-rotating discs described in Sengupta and Guha[16] has not been attempted here for the 1000 or so cases. Instead, we have exploited the expected axisymmetry of the flow field, by invoking the "axisymmetric swirl model" available in Fluent. However, before embarking upon a large scale study using this Fluent module (for which we did not have previous experience), we have assessed its predictions by comparing them against full three-dimensional computations (with $100 \times 190 \times 120$ grid points respectively in the r, θ, z directions[16]) for a limited number of cases. Table 2 shows the details of such a comparison. It can be seen that the axisymmetric computations can predict $\Delta\hat{p}_{io}$ within 0.01% and $\hat{W}$ within 0.02% of the respective values predicted by the three-dimensional simulations.

Figure 2 represents outline features of a typical flow-field between two consecutive discs of a Tesla disc turbine with axisymmetric inflow boundary condition. Figure 2(a) shows the absolute pathlines on the middle $r - \theta$ plane (at $z = b/2$) between the two discs. The results correspond to a steady state for which a pathline and a streamline drawn through a common point are superposed. The absolute pathlines are of spiral shape due to the simultaneous existence of radial as well as tangential velocity components (the z-component of velocity is zero on the middle plane). Various characteristics of pathlines are explained in Sengupta and Guha.[16] Figure 2(b) shows the variation in non-dimensional pressure, $\hat{p}$, within the inter-disc-spacing. It can be observed that the z-variation of $\hat{p}$ is negligible (for the representative small Ds). This flow feature is consistent with the reduced z-momentum equation $\partial p/\partial z \approx 0$ considered in Sengupta and Guha[12] for developing a simple theory. Figure 2(b) also exhibits the fact that $\hat{p}$ decreases in the negative r-direction i.e. from the inlet to the outlet. Figure 2(c) shows the variation in $\hat{U}_\theta$ within the inter-disc-spacing. The value of $\hat{U}_\theta$ is 1 on the disc surfaces (i.e. at $\hat{z} = 0$ and $\hat{z} = 1$) due to the

no slip condition. $\hat{U}_\theta$ increases towards the middle-plane i.e. towards $\hat{z} = 0.5$. Figure 2(c) shows $\hat{U}_\theta$ monotonically decreases towards the outlet (though there may be cases in which $\hat{U}_\theta$ initially decreases as one moves radially inward from the inlet but increases near the outlet[15]). Both the z and r variations in $\hat{U}_r$ are displayed in Figure 2(d). $\hat{U}_r$ is zero on the disc surfaces (i.e. at $\hat{z} = 0$ and $\hat{z} = 1$) due to the no slip condition. For the selected small value of Ds, the $z-$ profile of $\hat{U}_r$ is parabolic. $\hat{U}_r$ then increases monotonically towards the middle-plane i.e. towards $\hat{z} = 0.5$ as one moves away from either disc surface. However, a more complex $z-$ profile of $\hat{U}_r$ may be obtained when Ds is large. In the CFD simulations, we found that with increasing Ds, the z-profile of $\hat{U}_r$ would change from parabolic to flat to W-shaped. (These details are not reported here since the primary purpose of the present study is performance optimization of Tesla disc turbines, which is considered in section "Results and discussion".) The r-variation in $\hat{U}_r$ (for a parabolic profile) is such that $\hat{U}_r$ increases towards the outlet, as shown in Figure 2(d). This variation is consistent with the incompressible continuity equation since the flow cross-sectional area ($2\pi rb$) decreases with decreasing radius.

Results and discussion

Equations (16) to (20) show that there are five non-dimensional parameters $\hat{r}_o$, $\hat{b}$, γ, Ds, and α, which govern the fluid dynamics of the flow through co-rotating discs and the performance of a Tesla turbine. Each of these five input parameters is varied in the CFD simulations; and, Table 3 presents the ranges of their variations. It is to be recognized that the same dimensional quantity may be involved in more than one non-dimensional numbers. As an example, b, the gap between two consecutive discs, appears both in aspect ratio, $\hat{b}$, and dynamic similarity number, Ds. Therefore, a non-dimensional study, in which the effect of varying a non-dimensional number is to be found while keeping other non-dimensional numbers fixed, can be performed in a number of ways.
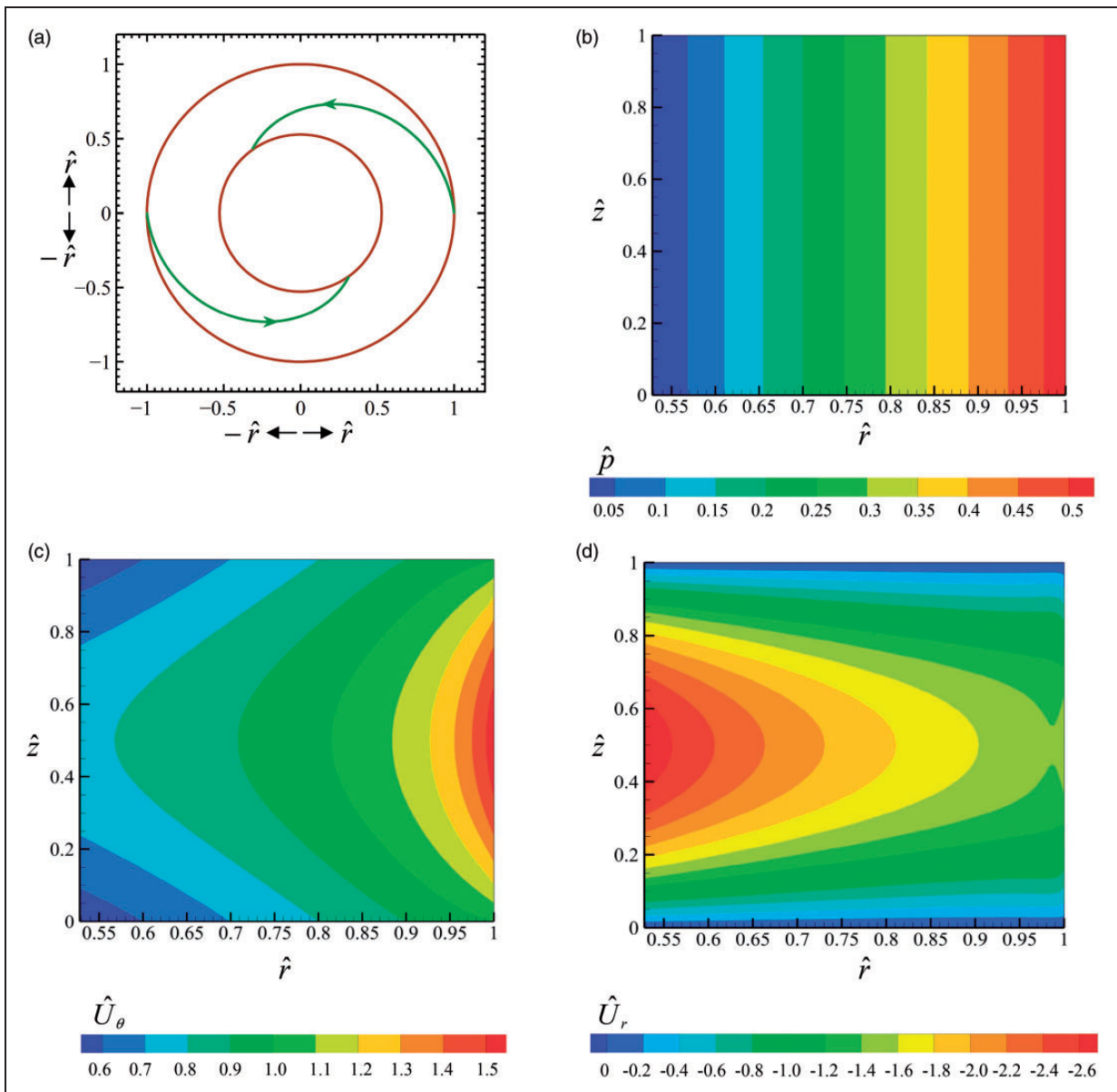
Figure 2. Flow field between two consecutive discs of a Tesla turbine: (a) absolute pathlines (i.e. the same as streamlines under steady state) calculated on the middle plane between the two discs; (b) contours of non-dimensional static pressure; (c) contours of non-dimensional absolute tangential velocity; (d) contours of non-dimensional radial velocity (for $\hat{r}_o = 0.528$, $\hat{b} = 0.0046$, $\gamma = 1.37$, $\alpha = 6.2°$, $Ds = 0.42$, and PVDI).

Table 3. Ranges of the tested input parameters for the present CFD simulations.

Input parameter	Symbol	Minimum value	Maximum value
Radius ratio	$\hat{r}_o$	0.3	0.7
Aspect ratio	$\hat{b}$	0.004	0.016
Flow angle at inlet	α	0.5°	10°
Tangential speed ratio at inlet	γ	0.4	4.7
Dynamic similarity number	Ds	0.15	2.5

Suppose we want to study the effect of dynamic similarity number. In a computational study, this can be achieved simply by altering the fluid viscosity μ, since equations (16) to (20) show that μ appears only in the definition of Ds. Therefore, Ds can be varied very simply by this method while keeping all other non-dimensional numbers fixed. This is the method adopted in the present study. On the other hand, if one is to embark upon an experimental study on the non-dimensional performance of a Tesla turbine, this method alone may not be sufficient or appropriate as the available values of μ will be restricted by the values of a real property of suitable fluids. Hence, a number of (raw) dimensional quantities may need to be simultaneously adjusted to vary Ds continuously while keeping other non-dimensional numbers fixed.

The role of radial pressure difference in determining the performance of a Tesla disc turbine is critically assessed in the following sections. The components of overall pressure difference are defined in section

"Components of radial pressure difference in a relative frame of reference" (equations (12) to (15)). These components are non-dimensionalized as follows

$$\Delta \hat{p}_{io,inertia} \equiv \Delta p_{io,inertia}/\rho \bar{U}_{\theta,i}^2$$

$$\Delta \hat{p}_{io,Coriolis} \equiv \Delta p_{io,Coriolis}/\rho \bar{U}_{\theta,i}^2$$

$$\Delta \hat{p}_{io,centrifugal} \equiv \Delta p_{io,centrifugal}/\rho \bar{U}_{\theta,i}^2 \qquad (31)$$

$$\Delta \hat{p}_{io,viscous} \equiv \Delta p_{io,viscous}/\rho \bar{U}_{\theta,i}^2$$

It is shown here how the overall pressure difference coefficient $\Delta \hat{p}_{io}$ (equation (22)) and the relative magnitudes of its various components (equation (31)) vary over a range of Ds (section "Role of dynamic similarity number (Ds)") and over a range of γ (section "Role of tangential speed ratio at inlet (γ)"). We have given emphasis not only on the overall magnitude of the radial pressure difference but also on the mechanisms of how this pressure difference takes place, since this understanding is of fundamental importance and may be the key to future improved designs.

Role of dynamic similarity number (Ds)

The effect of change in Ds on the performance of a Tesla turbine is investigated in this section, while keeping all other non-dimensional numbers fixed. The discussion given in this section therefore corresponds to a particular value of γ, i.e. $\gamma = 1.37$ (why this value of γ is selected here can be appreciated after the results of sections "Role of tangential speed ratio at inlet (γ)", "Role of aspect ratio ($\hat{b}$)", and "Role of radius ratio ($\hat{r}_o$)" are explained).

Figure 3 shows that the power coefficient $\hat{\dot{W}}$ increases with a decrease in Ds. The increase in $\hat{\dot{W}}$

may not necessarily imply an increase in the absolute value of power output $\dot{W}$. It is so because the flow parameters ρ and $|\bar{U}_{r,i}|$ in the denominator of $\hat{\dot{W}}$ are also present in the expression of Ds; and, the denominator of $\hat{\dot{W}}$ may vary with a change in Ds depending on which dimensional input quantities are altered to achieve the given change in Ds. Equation (20) shows that a possible way to decrease Ds, without varying the denominator of $\hat{\dot{W}}$, is to increase the dynamic viscosity μ. The physical interpretation is then that the power output $\dot{W}$ of a Tesla disc turbine can be increased by using a more viscous fluid. It is, however, established in the present study that even though the power coefficient continuously increases with decreasing Ds, there may be unacceptable penalty in the two other important parameters of performance—radial pressure drop and efficiency—if Ds is decreased below a critical value. The influence of Ds on $\Delta \hat{p}_{io}$ and η is therefore critically assessed below.

Figure 4 shows the variation of $\Delta \hat{p}_{io}$ and η with Ds. It can be seen that the curve corresponding to the variation of $\Delta \hat{p}_{io}$ is bucket-shaped. The magnitude of $\Delta \hat{p}_{io}$ is minimum at around $Ds = 0.56$. For both small and large values of Ds, $\Delta \hat{p}_{io}$ is large. On the other hand, the curve corresponding to η versus Ds is inverted bucket-shaped. The maximum η occurs approximately at $Ds = 0.43$. Any further increase or decrease in Ds leads to a decrease in η.

The variation of η versus Ds can be explained with the help of equation (30), Figure 3 ($\hat{\dot{W}}$ vs. Ds curve) and Figure 4 ($\Delta \hat{p}_{io}$ vs. Ds curve). First, consider equation (30). Equation (30) shows that η is the ratio of $\dot{W}$ to $Q(p_i + 0.5\rho(U_{\theta,i}^2 + U_{r,i}^2))$. Now, divide both numerator and denominator of equation (30) by $(\rho |\bar{U}_{r,i}|^3 r_i^2)$.
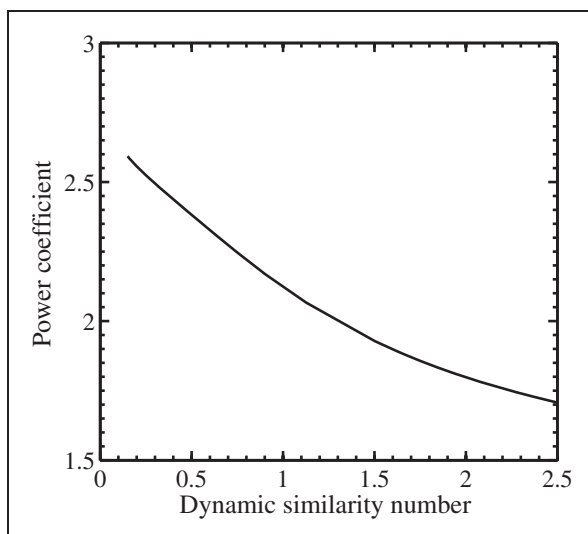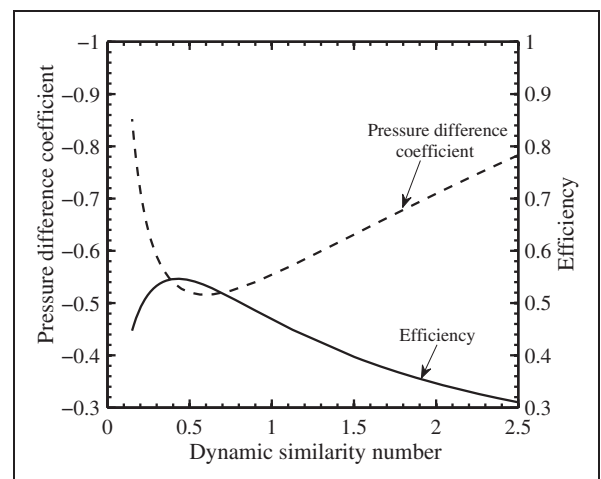

Figure 3. Variation in power coefficient $\hat{\dot{W}}$ with dynamic similarity number Ds obtained by the present CFD simulations (for $\hat{r}_o = 0.528$, $\hat{b} = 0.008$, $\gamma = 1.37$, $\alpha = 6.2°$, and PVDI).

Figure 4. Variation in pressure difference coefficient $\Delta \hat{p}_{io}$ and efficiency η with dynamic similarity number Ds obtained by the present CFD simulations. (For $\hat{r}_o = 0.528$, $\hat{b} = 0.008$, $\gamma = 1.37$, $\alpha = 6.2°$, and PVDI. Pressure differences are non-dimensionalized by $\rho \bar{U}_{\theta,i}^2$. Each curve contains data from 50 separate CFD simulations, with appropriate higher resolution close to the minima or maxima.)

As a result, the numerator becomes $\hat{\dot{W}}$ and the denominator becomes $C_1 \Delta \hat{p}_{io} + C_2$. In the present case, both C_1 and C_2 are constants. The curve corresponding to $\hat{\dot{W}}$ versus Ds shows that $\hat{\dot{W}}$ always decreases with an increase in Ds. On the other hand, the curve corresponding to $\Delta \hat{p}_{io}$ versus Ds shows that when Ds is greater than 0.56, $\Delta \hat{p}_{io}$ increases with an increase in Ds. Consequently, when $Ds > 0.56$ the variation of both $\Delta \hat{p}_{io}$ and $\hat{\dot{W}}$ causes a decrease in η. When Ds is less than 0.56, $\Delta \hat{p}_{io}$ tries to decrease η whereas, $\hat{\dot{W}}$ tries to increase η. The competition between $\Delta \hat{p}_{io}$ and $\hat{\dot{W}}$ is reflected in Figure 4 which shows that the maxima of η versus Ds curve occurs at a smaller Ds ($Ds = 0.43$) than the Ds corresponding to the minima of $\Delta \hat{p}_{io}$ versus Ds curve (i.e. $Ds = 0.56$). When Ds is less than 0.43, the effect of increase in $\Delta \hat{p}_{io}$ overtakes the effect of increase in $\hat{\dot{W}}$, therefore, η decreases.

Figure 5 shows the variation of $\Delta \hat{p}_{io}$ and its four components $\Delta \hat{p}_{io,inertia}$, $\Delta \hat{p}_{io,Coriolis}$, $\Delta \hat{p}_{io,centrifugal}$ and $\Delta \hat{p}_{io,viscous}$ with Ds. The following observations can be made from Figure 5. $\Delta \hat{p}_{io,centrifugal}$ does not vary with a change in Ds (Equations (14) and (31) show that $\Delta \hat{p}_{io,centrifugal}$ depends on $\hat{r}_o$ and γ. Both $\hat{r}_o$ and γ are fixed in this case.). Secondly, with an increase in Ds, the magnitudes of both $\Delta \hat{p}_{io,inertia}$ and $\Delta \hat{p}_{io,Coriolis}$ increase; whereas, the magnitude of $\Delta \hat{p}_{io,viscous}$ decreases. Thirdly, at a small value of Ds, the values of both $\Delta \hat{p}_{io,inertia}$ and $\Delta \hat{p}_{io,Coriolis}$ are small, whereas the value of $\Delta \hat{p}_{io,viscous}$ is large. Finally, at a large Ds,
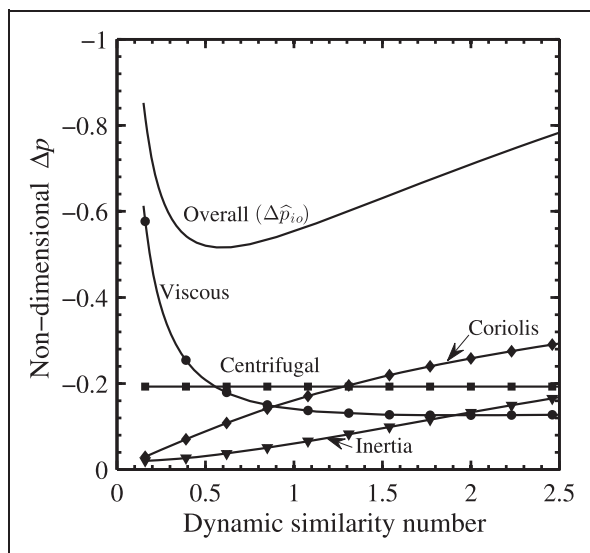
the magnitudes of both $\Delta \hat{p}_{io,inertia}$ and $\Delta \hat{p}_{io,Coriolis}$ overtakes the magnitude of $\Delta \hat{p}_{io,viscous}$.

It can be summarised that at a small value of Ds, the large magnitude of $\Delta \hat{p}_{io}$ occurs because of the large $\Delta \hat{p}_{io,viscous}$. On the other hand, at a comparatively greater Ds, a large magnitude of $\Delta \hat{p}_{io}$ occurs from a combined effect of $\Delta \hat{p}_{io,inertia}$, $\Delta \hat{p}_{io,Coriolis}$ and $\Delta \hat{p}_{io,centrifugal}$. Thus, the bucket-shape of $\Delta \hat{p}_{io}$ versus Ds curve, as shown in Figure 4, is obtained. The present study reveals that adding more and more friction either by reducing inter-disc-spacing or by using a fluid of higher viscosity may produce an adverse effect on the performance of a Tesla disc turbine. This is so because with an increase in friction, Ds decreases; and at a small Ds, $\Delta \hat{p}_{io}$ is large (i.e. for large $\Delta \hat{p}_{io,viscous}$). Figure 4 shows that the efficiency decreases rapidly below a critical value of Ds. (It is stated previously that although $\hat{\dot{W}}$ increases with a decrease in Ds there is a penalty when Ds is below a critical value.) A Tesla disc turbine is sometimes referred to as "friction turbine". However, the above detrimental role of friction regarding the performance of a Tesla turbine is not discussed in the previous literature.

Role of tangential speed ratio at inlet (γ)

The effect of change in γ on the performance of a Tesla turbine is investigated in this section. The study given in the previous section showed that the efficiency is maximum when $Ds = 0.43$. Therefore, Ds is kept fixed at this value ($Ds = 0.43$), as γ is varied. Additionally, $\hat{r}_o$, $\hat{b}$, and α are assumed to be fixed. γ is defined by equation (18): $\gamma = \bar{U}_{\theta,i}/(\Omega r_i)$. The absolute tangential velocity at the inlet of the rotor, $\bar{U}_{\theta,i}$, is fixed by the design of the nozzle and, r_i is fixed for a particular rotor. Therefore, in order to understand the fluid dynamics of the rotational flow, γ in this study is varied by altering the rotational speed Ω.

Figure 6 shows that decreasing γ (i.e. increasing Ω) up to a certain value leads to an increase in $\hat{\dot{W}}$. For further decrease in γ, $\hat{\dot{W}}$ decreases. Equation (28) shows that the power output $\dot{W}$ is a product of the rotational speed of the disc (Ω) and the torque produced by viscous drag (Γ_{shear}). For fixed geometry, fluid and $U_{\theta,i}$, Γ_{shear} decreases with an increase in Ω. Usually, the effect of increase in Ω overtakes the effect of decrease in Γ_{shear}, and hence the power output $\dot{W}$ increases with increasing Ω (i.e. decreasing γ). This trend may get reversed under flow reversal conditions (which happens for $\gamma < 1$, see Guha and Sengupta[13]) when a part of the disc near inlet, instead of producing power, absorbs power. Therefore, for $\gamma < 1$, a condition may reach such that any further decrease in γ decreases the power output $\dot{W}$. (Observe, in Figure 6, the variation of $\hat{\dot{W}}$ for $\gamma < 1$.)

Figure 6 also shows the variation of $\Delta \hat{p}_{io}$ with γ. It can be seen that $\Delta \hat{p}_{io}$ increases with a decrease in γ; and the rate of the increase in $\Delta \hat{p}_{io}$ is greater at comparatively smaller values of γ. The explanation behind

Figure 5. Predicted contribution of various forces to produce the overall pressure difference between outlet and inlet: effect of Ds. (CFD simulations are performed for $\hat{r}_o = 0.528$, $\hat{b} = 0.008$, $\gamma = 1.37$, $\alpha = 6.2°$, and PVDI. Pressure differences are non-dimensionalized by $\rho \bar{U}_{\theta,i}^2$. Each curve contains data from 50 separate CFD simulations, with appropriate higher resolution close to the minima. The bullets are used only for easy recognition of the various curves.)
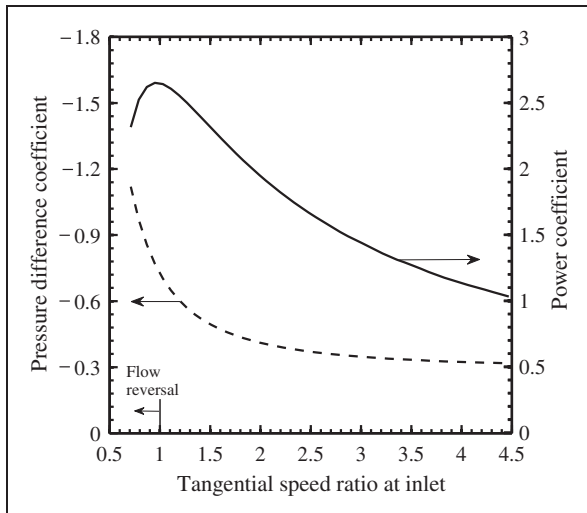
Figure 6. Variation in power coefficient $\hat{W}$ and pressure difference coefficient $\Delta\hat{p}_{io}$ with tangential speed ratio at inlet γ obtained by the present CFD simulations. (For $\hat{r}_o = 0.528$, $\hat{b} = 0.008$, $Ds = 0.43$, $\alpha = 6.2°$, and PVDI. Pressure differences are non-dimensionalized by $\rho\bar{U}_{\theta,i}^2$. Each curve contains data from 50 separate CFD simulations, with appropriate higher resolution close to the maxima in power coefficient.)
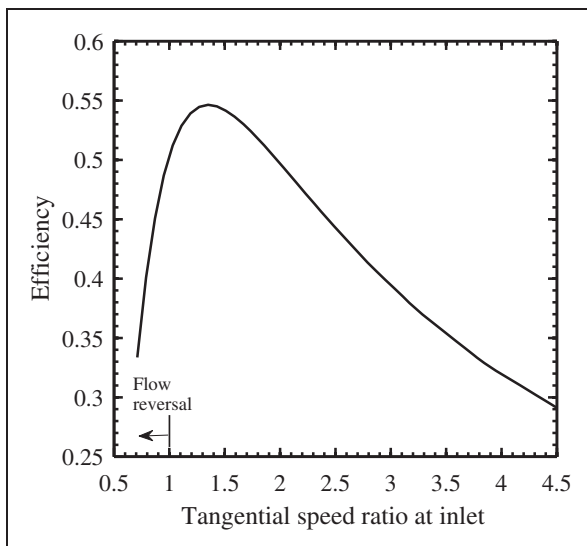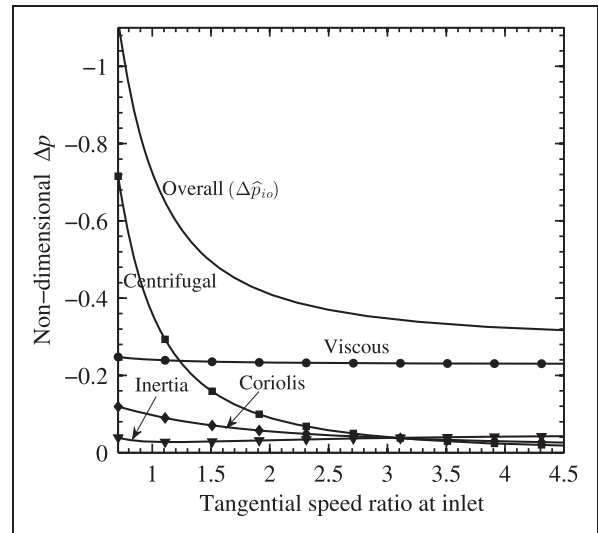Keys:– – –$\Delta\hat{p}_{io}$; —— $\hat{W}$).

Figure 8. Predicted contribution of various forces to produce the overall pressure difference between outlet and inlet: effect of γ. (CFD simulations are performed for $\hat{r}_o = 0.528$, $\hat{b} = 0.008$, $Ds = 0.43$, $\alpha = 6.2°$, and PVDI. Pressure differences are non-dimensionalized by $\rho\bar{U}_{\theta,i}^2$. Each curve contains data from 50 separate CFD simulations. The bullets are used only for easy recognition of the various curves.)

Figure 7. Variation in efficiency η with tangential speed ratio at inlet γ obtained by the present CFD simulations (for $\hat{r}_o = 0.528$, $\hat{b} = 0.008$, $Ds = 0.43$, $\alpha = 6.2°$, and PVDI).

such trend is given later in this paper (while discussing the contribution of various components of $\Delta\hat{p}_{io}$ over a range of γ).

Figure 7 shows the variation of η with γ. The curve corresponding to η versus γ is inverted bucket shaped. The maximum η occurs at $\gamma = 1.37$ (the value of γ corresponding to the maximum η is greater than 1 and close to 1). If γ is decreased below this optimum value, particularly when flow reversal occurs, η decreases steeply. Similarly, when γ is increased above the optimum value, η decreases considerably

(though may not be as steeply as before). Such variation in η may be explained in the following way. When γ is greater than 2, Figure 6 shows that, with an increase in γ, the rate of decrease in $\hat{W}$ is much greater than the rate of decrease in $\Delta\hat{p}_{io}$. Consequently, the value of η decreases. On the other hand, when γ is less than 1, $\Delta\hat{p}_{io}$ increases drastically. Moreover, with a decrease in γ, the rate of increase in $\hat{W}$ decreases when γ is close to 1; and, $\hat{W}$ starts decreasing when γ is less than 0.85. Thus, η is sufficiently small at $\gamma \sim 1$, and decreases rapidly when $\gamma < 0.85$.

Figure 8 shows the contribution of various components of $\Delta\hat{p}_{io}$ over a range of γ. The following observations can be made from Figure 8. $\Delta\hat{p}_{io,viscous}$ varies insignificantly as compared to the other components of $\Delta\hat{p}_{io}$. (This can be explained by equation (25), which shows that γ is not present in the viscous term. Moreover, it is found in the CFD simulations that the radial velocity field within the inter-disc-spacing of a Tesla turbine is weakly dependent on γ.) Secondly, the magnitude of $\Delta\hat{p}_{io,centrifugal}$ increases rapidly with a decrease in γ. At small γ, $\Delta\hat{p}_{io,centrifugal}$ is the major contributor. (Equations (14) and (31) show that $\Delta\hat{p}_{io,centrifugal}$ is inversely proportional to the square of γ. The rapid increase of $\Delta\hat{p}_{io}$ at small γ, as found in Figure 6, is because of the rapid increase of $\Delta\hat{p}_{io,centrifugal}$.) Finally, for the selected Ds, both $\Delta\hat{p}_{io,Coriolis}$ and $\Delta\hat{p}_{io,inertia}$ are small, which is consistent with the message contained in Figure 5. This figure also suggests that if the curves in Figure 8 were redrawn at a high value of Ds, then the inertial and Coriolis components of pressure drop

can be appreciably large. Returning to the computations of Figure 8, it is found that as γ decreases from a large value, the magnitude of $\Delta\hat{p}_{io,inertia}$ decreases and the magnitude of $\Delta\hat{p}_{io,Coriolis}$ increases, though both trends reverse below certain small values of γ (the reversal in $\Delta\hat{p}_{io,inertia}$ is visible in Figure 8, the reversal in $\Delta\hat{p}_{io,Coriolis}$ could be seen if the lower limit of abscissa is extended below 0.53).

$\Delta p_{io,Coriolis}$ depends on the product of V_θ and Ω (equation (13)). With a decrease in γ, the magnitude of $\Delta p_{io,Coriolis}$ increases mainly because of an increase in Ω, and below a certain γ, the magnitude of $\Delta p_{io,Coriolis}$ decreases mainly because of a decrease in $V_{\theta,i}$ ($V_{\theta,i}$ is the value of V_θ at inlet). However, while estimating $\Delta p_{io,Coriolis}$ one should also take the radial variation of V_θ into account because $\Delta p_{io,Coriolis}$ is an integrated value covering the full radial extent between the inlet and the outlet. Guha and Sengupta[13] explained the fluid dynamics for the radial variation of V_θ at various values of γ. They showed that, depending on the relative magnitude of various forces, two different trends are possible in the radial variation of V_θ. In one case, with decreasing radius from the inlet, V_θ decreases to a minimum at a certain radius (whose value depends on Ds and γ, and would be observable only if the value of this radius is greater than the outlet radius used in the particular design) and then onwards increases. This happens when γ is sufficiently greater than 1. In the other case, V_θ continuously increases with a decrease in radius (i.e. from inlet to outlet). This happens either when γ is less than 1 or when γ is close to 1.

The existence of the optimum values of γ for maximum power $\dot{W}$ (Figure 6) and for maximum efficiency η (Figure 7) can be explained from a simple theory. It has been postulated in Hoya and Guha[11] and demonstrated through present CFD simulations (Appendix 1) that $\Gamma_{shear} \approx c_1 - c_2\Omega$. The analytical expression for the torque, equation (29) which is valid for a small inter-disc spacing where a parabolic velocity distribution is a good assumption, shows that the variation of Γ_{shear} with Ω is exactly linear (Appendix 1). Therefore, $\dot{W} = \Gamma_{shear}\Omega = c_1\Omega - c_2\Omega^2$. The optimum γ for maximum power output is therefore obtained by setting $\partial\dot{W}/\partial\Omega = 0$. This gives, $\Omega_{optimum,\max power} = c_1/2c_2$. When appropriate values are substituted it is found that $\gamma_{optimum,\max power} = 0.96$; this compares well with $\gamma_{optimum,\max power} = 0.96$ determined directly through CFD simulations. Since, $\Delta\hat{p}_{io}$ changes mainly because of the centrifugal component at low value of γ (i.e. high Ω), the pressure difference would be approximately given by $\Delta p_{io} \approx c_3 + c_4\Omega^2$. For maximum η, $\partial\eta/\partial\Omega = 0$. This would set the optimum value of rotational speed, $\Omega_{optimum,\max\eta}$ (i.e. non-dimensional $\gamma_{optimum}$). When this algebra is carried out, $\Omega_{optimum,\max\eta} = \frac{ac}{b}[\sqrt{1+\frac{b}{a^2c}} - 1]$, where $a = c_2/c_1$, $b = c_4/c_1$, $c = [c_3 + 0.5\rho(U_{\theta,i}^2 + U_{r,i}^2)]/c_1$. When the values are substituted it is found that

$\gamma_{optimum,\max\eta} = 1.35$; this compares well with $\gamma_{optimum,\max\eta} = 1.37$ determined directly through CFD simulations.

Role of aspect ratio ($\hat{b}$)

In this study, we focus our attention to the two most important non-dimensional numbers that control the flow field and efficiency, namely Ds and γ. At the first thought, it appears that $\hat{b}$ should also play an important role since the relative proximity of two disc surfaces would influence the value of shear stress and hence the torque and work output. However, equation (20) shows that the expression of $\hat{b}$ is included in the definition of Ds. Since the systematic dimensional analysis of Guha and Sengupta[1] has produced both Ds and $\hat{b}$ as two separate non-dimensional numbers, we need to reflect on their separate roles. On the basis of a very large number of computational simulations, in which Ds and $\hat{b}$ were independently varied over respective relevant ranges, it was found that when $\hat{b}$ is varied but Ds is held constant (by making compensating changes in b, $|\bar{U}_{r,i}|$ and ν), there is only a little change in the non-dimensional flow field (e.g. in $\hat{U}_\theta$, $\hat{U}_r$, or $\hat{p}$ as a function of $\hat{z}$ and $\hat{r}$) within the co-rotating discs of a Tesla turbine. Results of these additional computations are not displayed in this paper since the non-dimensional curves corresponding to various $\hat{b}$ nearly superpose on one another. On the other hand, if $\hat{b}$ is fixed but Ds is varied then large changes happen both in the flow field and in the performance. Thus, we make the important conclusion that the primary role of aspect ratio $\hat{b}$ is contained in the dynamic similarity number Ds. The role of $\hat{b}$ as a separate non-dimensional number, independent of Ds, is secondary in determining the non-dimensional flow field. This subtle dynamics can be appreciated from a study of the three momentum equations (25) to (27) in which, outside Ds, $\hat{b}$ independently appears as a squared quantity. Since $\hat{b}$ for a practical Tesla turbine is a small quantity, square of $\hat{b}$ is even smaller. This provides the mathematical explanation for why the independent role of $\hat{b}$, outside Ds, on the flow field is secondary. A physical reasoning may be constructed as follows. Equation (20) shows that Ds is a product of the aspect ratio $\hat{b}$ and the term $|\bar{U}_{r,i}|b/\nu$. The term $|\bar{U}_{r,i}|b/\nu$ can be interpreted as a Reynolds number based on the average radial velocity at inlet and the inter-disc-spacing. Therefore, in order to keep Ds fixed, an increase in $\hat{b}$ must be accompanied by a corresponding decrease in the Reynolds number $|\bar{U}_{r,i}|b/\nu$, and vice versa. (As an example, if the aspect ratio $\hat{b}$ is increased by increasing the inter-disc-spacing b, then the Reynolds number can be decreased by increasing ν, i.e. by using a more viscous fluid.) Due to these two counteracting effects, the non-dimensional flow field does not change appreciably. For most computations reported here, it is assumed that $\hat{b} = 0.008$.

Having determined the effect of $\hat{b}$ on the flow field we turn our attention to its effect on the performance parameters. For the simplicity of argument, it is assumed that $\hat{b}$ is altered by altering b (keeping r_i fixed). The additional computations (mentioned above) showed that the pressure difference coefficient $\Delta\hat{p}_{io}$ and the efficiency η are nearly independent of $\hat{b}$, but the power coefficient $\hat{W}$ increases (nearly) linearly with increasing $\hat{b}$ (at fixed Ds). We have explained in the previous paragraph that $\hat{p}$ is nearly independent of $\hat{b}$, therefore $\Delta\hat{p}_{io}$ is also independent of $\hat{b}$. A casual glance at equations (28) and (29) may suggest that the power output would decrease with increasing b, since according to equation (29) b appears in the denominator of the torque Γ_{shear}. The explanation for why the opposite happens is quite subtle. Since the four other non-dimensional numbers, namely $\hat{r}_o$, γ, α, and Ds, are to be kept constant as $\hat{b}$ is varied, equations (16) to (20) show that the easiest way to achieve this is to keep all dimensional variables fixed except b and ν. In order to keep Ds fixed, ν (hence, μ for fixed ρ) must be varied such that $\mu \propto b^2$. Equations (29) and (28) then show why $\hat{W}$ increases (nearly) linearly with increasing $\hat{b}$. Since both $\hat{W} \propto b$ and $Q \propto b$, approximately, in equation (30), the efficiency η is nearly independent of $\hat{b}$.

Role of radius ratio ($\hat{r}_o$)

For saving space, a short summary of the effect of varying radius ratio, while keeping other non-dimensional numbers fixed ($Ds = 0.43$, $\gamma = 1.37$, $\hat{b} = 0.008$, $\alpha = 6.2°$), is given in Table 4. It can be concluded that, with decreasing $\hat{r}_o$ (i.e. with increasing radial extent of the disc surface), both pressure difference coefficient $\Delta\hat{p}_{io}$ and power coefficient $\hat{W}$ increase. As a result, the efficiency η shows a maxima at a certain value of $\hat{r}_o$. It can also be seen that, although there is an optimum value of $\hat{r}_o$ for maximum efficiency, the dependence of efficiency on radius ratio is rather weak.

Surface representation of efficiency (η)

In sections "Role of dynamic similarity number (Ds)" and "Role of tangential speed ratio at inlet (γ)", the

Table 4. Variation of performance parameters with radius ratio (for $Ds = 0.43$, $\gamma = 1.37$, $\alpha = 6.2°$, $\hat{b} = 0.008$, and PVDI).

$\hat{r}_o$	$\Delta\hat{p}_{io}$	$\hat{W}$	η
0.3	−0.919405	2.857994	0.469539
0.4	−0.718222	2.696741	0.515862
0.528	−0.532810	2.423864	0.546430
0.6	−0.445010	2.236899	0.550843
0.7	−0.333082	1.934666	0.539977

PVDI: parabolic velocity distribution at inlet.

subtle role of Ds and γ in determining the performance of a Tesla disc turbine is discussed. The performance curves, shown in both the sections, are obtained when either Ds is fixed or γ is fixed. In the present section, it is shown how the efficiency of a Tesla disc turbine varies when Ds and γ vary simultaneously. An initial survey of such calculations was performed at various values of radius ratio $\hat{r}_o$; from such calculations it is established that $\hat{r}_o = 0.63$ gives the highest value of maximum efficiency. Now, several hundreds of further computations were performed at finer intervals in Ds and γ, while keeping the three other non-dimensional numbers fixed ($\hat{r}_o = 0.63$, $\hat{b} = 0.008$, $\alpha = 6.2°$). Figure 9 shows a surface, which represents the variation of efficiency over a range of Ds and γ. Thus, the peak of the surface indicates the point of maximum efficiency over the range of Ds and γ. The maximum efficiency ($\eta_{max} = 0.552$) is attained at $Ds = 0.39$ and $\gamma = 1.45$. In course of the present investigation, it is found that it is not possible to achieve another maxima by any further changes in Ds, γ, $\hat{r}_o$ or $\hat{b}$, so long as α is kept fixed (the effect of varying α is shown in section "Role of flow angle at inlet (α)").

Reflection on real designs

Hoya and Guha[11] reported a flexible test rig in which it was possible to vary, among many of the input variables, the inter-disc-spacing b. In their experimental set up, it is possible to vary Ds within a wide range, which contains the optimum values of Ds described in previous sections. The minimum value of Ds used in the experiment of Lemma et al.[10] is, however, approximately 3.6. This value is large compared to
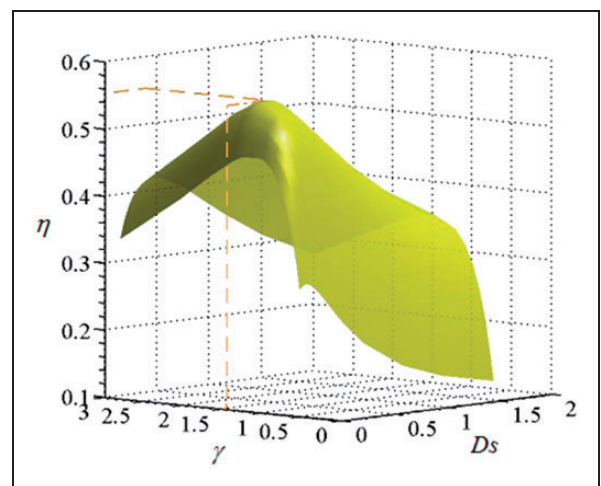

Figure 9. A surface representation of efficiency η of a Tesla disc turbine over a range of dynamic similarity number Ds and tangential speed ratio at inlet γ: prediction of present CFD simulations. (For $\hat{r}_o = 0.63$, $\hat{b} = 0.008$, $\alpha = 6.2°$ and PVDI. About 400 separate CFD simulations are performed to construct the surface.)

the optimum value found in the present study. Achievable modification in the fewest parameters that can bring the Ds value close to optimum is discussed below.

Let us maintain the dimensions of the rotor (i.e. $r_i = 25$ mm, $r_o = 13.2$ mm, $\hat{r}_o = 0.528$), and the same fluid (i.e. air with $\mu = 1.79 \times 10^{-5}$ kg/(ms) and $\rho = 1.225$ kg/m^3). Lemma et al.[10] reported the performance of their turbine at various inlet gauge pressure conditions. Now, consider a particular case (among these cases) for which the inlet gauge pressure is 0.113 bar. For this case, the values of absolute fluid velocities at inlet (i.e. $\bar{U}_{\theta,i} = 106$ m/s, $|\bar{U}_{r,i}| = 11.5$ m/s, $\alpha = 6.2°$) are obtained by the method described in Sengupta and Guha.[12] The present study given in sections "Role of dynamic similarity number (Ds)" and "Role of tangential speed ratio at inlet (γ)" showed that, with these values of α and $\hat{r}_o$, a maximum efficiency of $\eta_{\max} = 0.546$ can be obtained if $Ds = 0.43$ and $\gamma = 1.37$ are maintained. These can be achieved with $\Omega = 3095$ rad/s and $b = 117$ μm (which corresponds to $\hat{b} = 0.0047$).

Role of flow angle at inlet (α)

The collected wisdom accrued from the design experience of Tesla turbines over many years is that, for obtaining a good performance, the fluid should enter the rotor nearly tangentially. The detailed experimental study reported in McGarey and Monson,[22] in which the nozzle angle or the flow angle at inlet to the rotor was systematically varied, also concluded the same. For all computations described so far in this paper, we have assumed $\alpha = 6.2°$ (i.e. 0.11 radian), the value adopted in the design of Lemma et al.,[10] see previous section. In this section, we therefore undertake a computational study of the effect of varying α for the sake of completeness.

Figure 10 shows how the computed efficiency depends on α. It is found that the computed efficiency increases continuously with decreasing α. It should be mentioned that the present computations are performed for the isolated rotor; one may need to consider the whole assembly as the computational domain when α is small. In order to keep the same mass flow rate as α is varied, the radial velocity at inlet $U_{r,i}$ is kept constant in the present computations. Since, $\tan \alpha \approx \alpha$, when α is small and expressed in radian, $U_{\theta,i} \propto 1/\alpha$. It is expected that, under the circumstances, $\dot{W}$ will scale with $U_{\theta,i}^2$. It is therefore predicted that $\dot{W} \propto 1/\alpha^2$, i.e. if the flow angle at inlet to the rotor is halved, the power output would be doubled. This theoretical prediction is borne out by the CFD simulations. The variation of $\dot{W}$ versus α would therefore be steeper at small angle, since the same change in angle, $\Delta\alpha$, would represent a larger fraction of α when α is smaller. The special form of abscissa in Figure 10 is chosen to display finer resolution at small values of α.
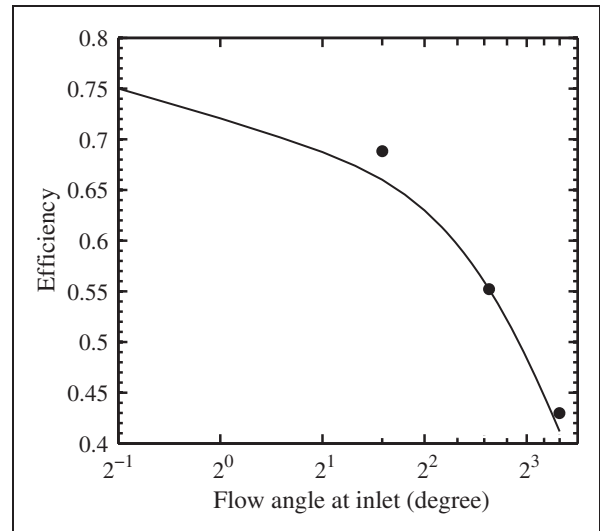

Figure 10. Variation in efficiency η with flow angle at inlet α (in degree) obtained by the present CFD simulations (for $\hat{r}_o = 0.63$, $\hat{b} = 0.008$, $\gamma = 1.45$, and PVDI). Keys: —— with $Ds = 0.39$; ● with optimum values of Ds at respective angles.
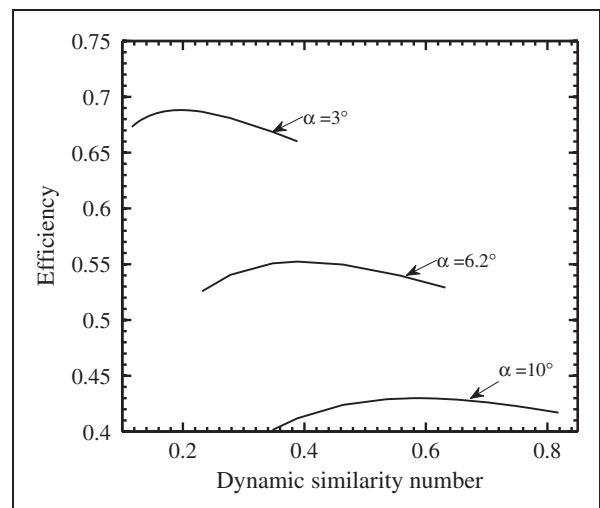

Figure 11. Variation of efficiency η in the neighborhood of the optimum dynamic similarity number Ds: prediction of present CFD simulations at three different flow angles at inlet (for $\hat{r}_o = 0.63$, $\hat{b} = 0.008$, $\gamma = 1.45$, and PVDI).

The computations shown in Figure 10 are performed at fixed values of Ds and γ. In order to complete the present non-dimensional study, two more questions need to be answered: (i) how the optimum values of Ds and γ change with varying angle α, and (ii) how the efficiency behaves in the neighborhoods of optimum values of Ds and γ. Many further computations showed that the optimum value of γ does not appreciably change with varying α, the optimum remaining at $\gamma = 1.45$ (section "Surface representation of efficiency (η)"). The optimum of Ds, however, decreases with decreasing α. The variation of η with Ds, in the neighbourhood of respective optimum Ds,

is shown in Figure 11 for three different values of α. The optimum values of Ds and maximum values efficiency are (0.2, 0.688), (0.39, 0.552), and (0.59, 0.43) respectively at $\alpha = 3°$, $\alpha = 6.2°$, and $\alpha = 10°$. The three points are also superposed (as filled circles) in Figure 10 so that one can appreciate the effect of optimizing Ds at various angles α.

Figure 11 shows that the efficiency curves are reasonably flat, particularly at higher angles α, in the neighborhood of optimum Ds. This has design implication in that the penalty for small deviation from the exact optimum value of Ds may not be too severe on the efficiency.

Conclusion

A systematic CFD study is presented for understanding the flow through co-rotating discs and for predicting the performance of a Tesla disc turbine. The full benefit of similitude and scaling is extracted by expressing the results and analyses in terms of carefully formulated non-dimensional numbers—five input parameters ($\hat{r}_o$, $\hat{b}$, γ, α, Ds) and three output parameters ($\hat{W}$, $\Delta\hat{p}_{io}$, η). A quantitative methodology is established to design the best possible rotor of a Tesla disc turbine. Many subtle flow physics (e.g. the dual role of fluid friction, the identification of Ds, γ, and α as the three most important non-dimensional input parameters, the secondary role of aspect ratio as a separate quantity independent of the dynamic similarity number in determining flow field and efficiency, and the variation in the four fundamental components of the radial pressure difference) are critically explained for the first time in this paper. The work establishes a systematic design methodology for the optimum selection of input parameters for a Tesla disc turbine that would satisfy practical constraints and deliver high value of power and efficiency. As an illustrative example (with $\hat{r}_o = 0.63$), it is shown that for an inlet flow angle $\alpha = 6.2°$, the maximum rotor efficiency ($\eta_{max} = 0.552$) is obtained when $Ds = 0.39$ and $\gamma = 1.45$. At an inlet flow angle $\alpha = 3°$, an increased maximum rotor efficiency ($\eta_{max} = 0.688$) may be obtained with the following optimum combinations of Ds and γ: $Ds = 0.2$, $\gamma = 1.45$.

The dependence of the fluid dynamics and performance on the input variables such as Ds, γ, and $\hat{b}$ has been determined here through a comprehensive set of computations which involve about 1000 separate simulations, each run to a high degree of convergence (the "scaled" residual for all conserved variables is set as 10^{-10}, which is much smaller than what is normally set in much of the reported CFD work). This comprehensiveness and precision have helped us to formulate generic principles and identify subtle physical mechanisms.

Thus, for example, we have given emphasis not only on the overall magnitude of the radial pressure difference but also on the mechanisms of how this pressure difference takes place. It is established that $\Delta\hat{p}_{io,viscous}$ depends predominately on Ds; $\Delta\hat{p}_{io,centrifugal}$ depends predominately on γ; and $\Delta\hat{p}_{io,inertia}$ and $\Delta\hat{p}_{io,Coriolis}$ depends on both Ds and γ (see Figures 5 and 8). Such understanding is of fundamental importance and may be the key to future improved designs.

In addition to the computational optimization, the analytical route is also taken wherever possible for deeper physical interpretation. As an example, simple analytical formulae for the optimum values of γ (for maximum power or efficiency) are derived, the predictions of which match well with the numerically determined values.

Usually the Tesla disc turbine is described as a "friction turbine" implying the positive role played by fluid friction since it increases the power output. The present study, for the first time, establishes the qualitative and quantitative cost of fluid friction and how the optimum design evolves as a balance between this dual role of friction in the Tesla disc turbine. It is shown that, as Ds decreases, although the power coefficient $\hat{W}$ continuously increases, the magnitude of pressure difference coefficient $\Delta\hat{p}_{io}$ (which appears in the denominator of efficiency η) passes through a minima, primarily for a large combined value of $\left|\Delta\hat{p}_{io,Coriolis}\right|$, $\left|\Delta\hat{p}_{io,inertia}\right|$, and $\left|\Delta\hat{p}_{io,centrifugal}\right|$ at large values of Ds and for a large increase in $\left|\Delta\hat{p}_{io,viscous}\right|$ at small values of Ds. As γ decreases, the power coefficient $\hat{W}$ increases (until the power curve passes through a maxima when γ is close to unity), but the magnitude of the pressure difference coefficient $\Delta\hat{p}_{io}$ also increases, primarily for a large increase in $\left|\Delta\hat{p}_{io,centrifugal}\right|$ at small values of γ. The balance between these two opposing effects of fluid friction gives rise to the optimum values of Ds and γ that maximize η.

References

1. Guha A and Sengupta S. Similitude and scaling laws for the rotating flow between concentric discs. *Proc IMechE, Part A: J Power and Energy* 2014; 228: 429–439.
2. Tesla N. *Turbine*. US Patent 1 061 206, 1913.
3. Guha A and Smiley B. Experiment and analysis for an improved design of the inlet and nozzle in Tesla disc turbines. *Proc IMechE, Part A: J Power and Energy* 2010; 224: 261–277.
4. Rice W. An analytical and experimental investigation of multiple-disk turbines. ASME Trans *J Eng Power* 1965; 87: 29–36.

5. Rice W. Tesla turbomachinery. In: Logan E (ed.) *Handbook of turbomachinery*. New York: Marcel Dekker, 2003, pp.861–874.

6. Guha A. Optimisation of aero gas turbine engines. *Aeronaut J* 2001; 105: 345–358.

7. Guha A. Performance and optimization of gas turbines with real gas effects. *Proc IMechE, Part A: J Power and Energy* 2001; 215: 507–512.

8. Guha A. Jump conditions across normal shock waves in pure vapour-droplet flows. *J Fluid Mech* 1992; 241: 349–369.

9. Guha A. Structure of partly dispersed normal shock waves in vapour-droplet flows. *Phys Fluids A* 1992; 4: 1566–1578.

10. Lemma E, Deam RT, Toncich D, et al. Characterisation of a small viscous flow turbine. *J Exp Therm Fluid Sci* 2008; 33: 96–105.

11. Hoya GP and Guha A. The design of a test rig and study of the performance and efficiency of a Tesla disc turbine. *Proc IMechE, Part A: J Power and Energy* 2009; 223: 451–465.

12. Sengupta S and Guha A. A theory of Tesla disc turbines. *Proc IMechE, Part A: J Power and Energy* 2012; 226: 650–663.

13. Guha A and Sengupta S. The fluid dynamics of the rotating flow in a Tesla disc turbine. *Eur J Mech B* 2013; 37: 112–123.

14. Romanin VD and Carey VP. An integral perturbation model of flow and momentum transport in rotating microchannel with smooth or microstructured wall surfaces. *Phys Fluids* 2011; 23: 082003–1:11.

15. Guha A and Sengupta S. The fluid dynamics of work transfer in the non-uniform viscous rotating flow within a Tesla disc turbomachine. *Phys Fluids* 2014; 26: 033601–1:27.

16. Sengupta S and Guha A. Analytical and computational solutions for three-dimensional flow-field and relative pathlines for the rotating flow in a Tesla disc turbine. *Comput Fluids* 2013; 88: 344–353.

17. Leaman AB. *The design, construction and investigation of a Tesla turbine*. MS Thesis, University of Maryland, USA, 1950.

18. Armstrong JH. *An investigation of the performance of a modified Tesla turbine*. PhD Thesis, Georgia Institute of Technology, USA, 1952.

19. Beans EW. *Performance characteristics of a friction disc turbine*. PhD Thesis, Pennsylvania State University, USA, 1961.

20. North RC. *An investigation of the Tesla turbine*. PhD Thesis, University of Maryland, USA, 1969.

21. Ladino AFR. *Numerical simulation of the flow field in a friction-type turbine (Tesla turbine)*. PhD Thesis, National University of Colombia, Colombia, 2004.

22. McGarey S and Monson P. *Performance and efficiency of disk turbines*. MEng Research Project Report (Advisor: A Guha), Report No. 1203, Aerospace Engineering Department, University of Bristol, UK, 2007.

23. Hoya GP. *Performance and efficiency of disk turbines*. MEng Research Project Report (Advisor: A Guha), Report No. 1277, Aerospace Engineering Department, University of Bristol, UK, 2008.

24. Smiley B. *Performance and efficiency of the nozzle in a Tesla disk turbine*. MEng Research Project Report (Advisor: A Guha), Report No. 1294, Aerospace Engineering Department, University of Bristol, UK, 2009.

25. Romanin VD. *Theory and performance of Tesla turbines*. PhD Thesis, University of California, USA, 2012.

26. von Kármán T. Über Läminare und turbulence Reibung. *Z Angew Math Mech* 1921; 1: 233–252.

27. Zandbergen PJ and Dijkstra D. Von Kármán swirling flows. *Annu Rev Fluid Mech* 1987; 19: 465–491.

28. Lingwood RJ. Absolute instability of the Ekman layer and related rotating flows. *J Fluid Mech* 1997; 331: 405–428.

29. Davies C and Carpenter PW. Global behaviour corresponding to the absolute instability of the rotating-disc boundary layer. *J Fluid Mech* 2003; 486: 287–329.

30. Batchelor GK. Note on a class of solutions of the Navier-Stokes equations representing steady rotationally-symmetric flow. *Quart J Mech Appl Math* 1951; 4: 29–41.

31. Stewartson K. On the flow between two rotating coaxial disks. *Proc Camb Phil Soc* 1953; 49: 333–341.

32. van Eeten KMP, van der Schaaf J, Schouten JC, et al. Boundary layer development in the flow field between a rotating and a stationary disk. *Phys Fluids* 2012; 24: 033601–1:18.

33. Poncet S, Chauve MP and Schiestel R. Batchelor versus Stewartson flow structures in a rotor-stator cavity with throughflow. *Phys Fluids* 2005; 17: 075110.

34. Holodniok M, Kubíček M and Hlaváček V. Computation of the flow between two rotating coaxial disks: Multiplicity of steady-state solutions. *J Fluid Mech* 1981; 108: 227–240.

35. Tzeng HM and Humphrey JA. Corotating disk flow in an axisymmetric enclosure with and without a bluff body. *Int J Heat Fluid Flow* 1991; 12: 194–201.

36. Gauthier G, Gondret P, Moisy F, et al. Instabilities in the flow between co- and counter-rotating disks. *J Fluid Mech* 2002; 473: 1–21.

37. *Fluent 6.3 User's guide*. Lebanon, NH, USA: Fluent Inc., 2006.

Appendix

Notation

b	spacing between two discs (m)
$\hat{b}$	aspect ratio, $\hat{b} \equiv b/r_i$
Ds	dynamic similarity number, $Ds \equiv (b/r_i)(|\bar{U}_{r,i}|b/\nu)$
g	acceleration due to gravity (m/s^2)
p	pressure (gauge value) (Pa)
p'	modified pressure, $p' \equiv p - \rho g_z z$ (Pa)
$\hat{p}$	non-dimensional gauge pressure, $\hat{p} \equiv p/\rho \bar{U}_{\theta,i}^2$
r	radius (m)
$\hat{r}$	non-dimensional radius, $\hat{r} \equiv r/r_i$
$\hat{r}_o$	radius ratio, $\hat{r}_o \equiv r_o/r_i$

U	absolute velocity of fluid (m/s)
$\hat{U}_\theta$	non-dimensional U_θ, $\hat{U}_\theta \equiv U_\theta/\Omega r_i$
$\hat{U}_r$	non-dimensional U_r, $\hat{U}_r \equiv U_r/|\bar{U}_{r,i}|$
V	relative velocity of fluid (m/s)
$\dot{W}$	power output (W)
$\hat{\dot{W}}$	power coefficient, $\hat{\dot{W}} \equiv \dot{W}/(\rho|\bar{U}_{r,i}|^3 r_i^2)$
z	height above the lower disc surface (m)
$\hat{z}$	non-dimensional z, $\hat{z} \equiv z/b$
α	flow angle at inlet, $\alpha \equiv \tan^{-1}(|\bar{U}_{r,i}|/\bar{U}_{\theta,i})$
Δp_{io}	overall pressure difference between outlet and inlet (Pa)
$\Delta \hat{p}_{io}$	pressure difference coefficient, $\Delta \hat{p}_{io} \equiv \Delta p_{io}/(\rho \bar{U}_{\theta,i}^2)$
γ	tangential speed ratio at inlet, $\gamma \equiv \bar{U}_{\theta,i}/(\Omega r_i)$
Γ_{shear}	torque produced by one side of a single disc (N m)
η	efficiency
θ	azimuthal direction in cylindrical co-ordinate system (rad)
μ	viscosity of the working fluid (kg/m s)
ν	kinematic viscosity of working fluid (m²/s)
ρ	density of the working fluid (kg/m³)
Ω	rotational speed of the disc (rad/s)

Subscript

i	at rotor inlet
o	at rotor outlet
r	component along the r-direction
z	component along the z-direction
θ	component along the θ-direction

Superscript

$\overline{()}$	sectional-averaged flow variables, $\overline{X}(r) \equiv (1/b)\int_0^b X(r)\,dz$

Appendix I

Theoretical derivation of the linear relationship between Γ_{shear} and Ω

The tangential speed ratio at inlet is defined by the equation $\gamma = \bar{U}_{\theta,i}/\Omega r_i$. It was mentioned in section "Role of tangential speed ratio at inlet (γ)" that, γ in this study is varied by altering the rotational speed Ω. In the same section, the existence of the optimum values of γ for maximum power $\dot{W}$ (Figure 6) and for maximum efficiency η (Figure 7) has been explained from a simple theory. The presented theory is based on the relation $\Gamma_{shear} \approx c_1 - c_2\Omega$,
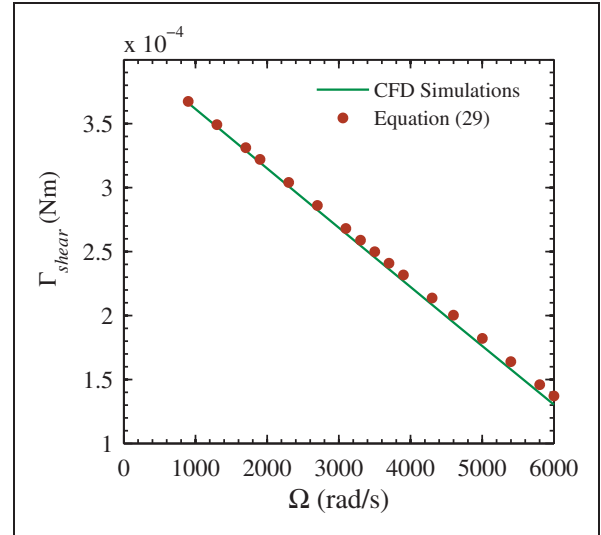

Figure 12. Variation of the torque produced by one side of a single disc of a Tesla turbine (Γ_{shear}) with the rotational speed of the disc Ω: predictions of present CFD simulations and equation (29) (for $r_i = 0.025$ m, $r_o = 0.0132$ m, b=116 μm, $\bar{U}_{\theta,i} = 106$ m/s, $\bar{U}_{r,i} = -11.5$ m/s, air as working fluid ($\rho = 1.225$ kg/m³ and $\mu = 1.79 \times 10^{-5}$ kg/m·s), and PVDI).

which has been postulated in Hoya and Guha.[11] The following analysis gives a mathematical derivation of this linear relationship by using equation (29).

From equation (8), $\overline{V}_{\theta,i}$ can be expressed as

$$\overline{V}_{\theta,i} = \overline{U}_{\theta,i} - \Omega r_i \tag{32}$$

Using the definition of γ (equation (18)), we have

$$\overline{V}_{\theta,i} = (\gamma - 1)\Omega r_i \tag{33}$$

Substituting the expression of $\overline{V}_{\theta,i}$ in equation (29), the following expression for Γ_{shear} is obtained

$$\Gamma_{shear} = \frac{12\pi\mu(\gamma-1)\Omega r_i^4}{b}\left[\frac{Ds}{12(\gamma-1)}(1-\hat{r}_o^2) + \frac{Ds}{10}\left(1 - \frac{Ds}{6(\gamma-1)}\right)F\right] \tag{34}$$

where

$$F = \left\{1 - \exp\left[-\frac{5}{Ds}(1-\hat{r}_o^2)\right]\right\} \tag{35}$$

Using the definition $\gamma = \bar{U}_{\theta,i}/\Omega r_i$, equation (34) can be expressed as

$$\Gamma_{shear} = k_1\Omega + k_0 - k_2\Omega - k_3\Omega \tag{36}$$

where, $k_0 = \frac{6\pi\mu r_i^3 \bar{U}_{\theta,i}}{5b} DsF$

$$k_1 = \frac{\pi \mu r_i^4}{b}(1 - \hat{r}_o^2)Ds$$

$$k_2 = \frac{6\pi \mu r_i^4}{5b}DsF$$

and, $k_3 = \frac{\pi \mu r_i^4}{5b}(Ds)^2 F$

Therefore, one can write $\Gamma_{shear} = c_1 - c_2\Omega$, where, $c_1 = k_0$ and $c_2 = k_2 + k_3 - k_1$.

It is also possible to determine the relation between Γ_{shear} and Ω directly from the many CFD simulations conducted here. Figure 12 shows that the prediction of the analytical theory, equation (29), is in good agreement with the CFD results.